MTLA 30 (2023) 101823

Contents lists available at ScienceDirect

Materialia

journal homepage: www.elsevier.com/locate/mtla

Functional properties and shape memory effect of Nitinol manufactured via electron beam powder bed fusion

Alexander Fink [a,*], Zongwen Fu [a], Carolin Körner [a,b]

[a] Joint Institute of Advanced Materials and Processes of Friedrich-Alexander Universität Erlangen-Nürnberg, Dr.-Mack-Straße 81, Fürth 90762, Germany
[b] Chair of Materials Science and Engineering for Metals of Friedrich-Alexander Universität Erlangen-Nürnberg, Martensstraße 5, Erlangen 91058, Germany

ARTICLE INFO

Keywords:
Shape memory effect (SME)
Martensitic phase transformation
NiTi
Thermal and mechanical cycling
Powder bed fusion - electron beam (PBF-EB)

ABSTRACT

Ti-rich Nitinol (NiTi) is characterized by its functional properties to restore its original shape after deformation due to a temperature-induced reversible martensitic phase transition. In this study, dense Ti-rich Nitinol free of cracks is successfully produced by means of Electron Beam Powder Bed Fusion (PBF-EB). The martensitic phase transition behavior of the as-built NiTi parts and powder is analyzed using Differential Scanning Calorimetry (DSC) analysis. To gain a deep understanding of the DSC results, segregation during solidification is thermodynamically studied (CALPHAD). The PBF-EB-fabricated NiTi shows a microstructure containing fine columnar grains and numerous precipitates, whose influence on the tensile properties at room temperature is discussed. Furthermore, the one-way and two-way shape memory effects of PBE-EB-produced NiTi are investigated using an innovative experimental setup based on thermomechanical training.

1. Introduction

Shape Memory Alloys (SMA), being able to remember their original form after deformation when the temperature rises, are used in a wide range of applications [1]. The binary alloy Nitinol (NiTi) is the most widely used material system in this class, since it can restore strains up to 8%. The binary NiTi exhibits not only the One-Way Shape Memory Effect (OWSME), but also superelasticity and Two-Way Shape Memory Effect (TWSME) being adjustable when varying the Ni-content of the alloy and applying a thermo-mechanical treatment [2]. Due to the good biocompatibility and excellent damping properties of NiTi, its applications in the biomedical area are well established [3]. Additionally, these unique Shape Memory Effects (SMEs) exhibit potential application prospects in the realm of aerospace [4], robotics [5], and chemical reactors [6].

The combination of NiTi with Additive Manufacturing (AM) opens up a new field allowing for innovative and customized designs as well as near-net shape manufacturing, being barely realizable using conventional fabrication techniques [2,7]. This can be advantageous since the machining of NiTi leads to high tool wear that can be minimized when using AM [8]. The commonly used AM process for NiTi is Laser Powder Bed Fusion (PBF-L); however, problems of crack formation due to residual stresses or embrittlement due to the oxygen pickup were observed [3,9]. The high preheating temperatures during Electron Beam Powder Bed Fusion (PBF-EB) can suppress crack formation which can occur in AM processes [2,9]. In addition, due to the high vacuum level, the oxygen pickup could be less prominent in PBF-EB [7]. Compared to previous studies focusing on superelastic Ni-rich NiTi fabricated via PBF-EB [10–12], this work is committed to investigating the SME using Ti-rich NiTi for PBF-EB. NiTi with a Ti-content of higher than 51 at.% is not as sensitive to the change in functional properties depending on probable Ni-loss caused by evaporation during PBF-EB [13]. Nevertheless, the martensitic phase transition and the resulting shape memory of NiTi depend not only on the overall Ni-content but also on other factors (e.g., the rapid solidification and precipitation of Ti_2Ni or Ti-rich oxygen complex phases) [14].

The main goals of this study are to understand the generation mechanism of the microstructural features of PBF-EB-produced Ti-rich NiTi in the as-built state and the powder as well as the influence of the microstructure on the martensitic phase transformation with the resulting functional properties. To reach these goals, a PBF-EB processing window was first developed for the fabrication of dense Ti-rich NiTi. The as-built NiTi and powders in different aging states showed different microstructural properties. Owing to these differences in the microstructure, different phase transition temperatures were observed, which were additionally discussed based on thermodynamic

* Corresponding author.
E-mail address: alexander.fink@fau.de (A. Fink).

https://doi.org/10.1016/j.mtla.2023.101823
Received 2 June 2023; Accepted 14 June 2023
Available online 17 June 2023
2589-1529/© 2023 The Authors. Published by Elsevier B.V. on behalf of Acta Materialia Inc. This is an open access article under the CC BY license (http://creativecommons.org/licenses/by/4.0/).

calculations (CALPHAD). Furthermore, based on tensile tests, the mechanical properties of the as-built Ti-rich NiTi at room temperature were investigated. Finally, the reversible one-way and two-way memory strains were studied using unique thermomechanical cycling tests developed in this work.

2. Experimental

Argon-atomized pre-alloyed Ti-rich NiTi powder provided by Eckart TLS GmbH (Bitterfeld-Wolfen, Germany) was used for PBF-EB in this work. The chemical composition of the powder is shown in Table 2. This chemical composition was analyzed using Inductively Coupled Plasma Atomic Emission Spectroscopy (ICP-AES, Ciros CCD, Spectro Analytical Instruments GmbH, Kleve, Germany) and the oxygen content was measured via carrier gas hot extraction method (EMGA-920, HORIBA Ltd, Kyoto, Japan). In the following study, the powder, being sieved and recycled after 20 PBF-EB process cycles, is called "used powder"; during each PBF-EB process cycle, the powder bed was preheated. The shape and surface quality of the NiTi powder were characterized through an optical microscope (Axio M1m Imager, Carl Zeiss AG, Oberkochen, Germany) and a Scanning Electron Microscope (SEM Quanta 450, FEI, Oregon, USA). According to SEM, the powder particles exhibited spherical morphology with a small number of satellites; simultaneously, based on the laser diffraction analysis (Mastersizer 3000, Malvern Panalytical GmbH, Kassel, Germany), the NiTi powder showed a particle size ranging between 45 μm and 125 μm (D_{10}=45.0 μm, D_{50}=64.4 μm and D_{90}=89.1 μm). The local chemical composition of the cross-sections was investigated using Electron Probe Micro Analysis (EPMA, JXA 8100, Jeol, Tokyo, Japan) after grinding, polishing, and ion milling (EM TIC 3X, Leica Microsystems, Wetzlar, Germany). In order to investigate the phase transition temperatures, Differential Scanning Calorimetry analysis (DSC, Netzsch, Selb, Germany) of fresh and used powders as well as printed solid parts was performed in a temperature range from -100 °C to 150 °C with a constant heating and cooling rate of 10 K/min. To determine the processing window for PBF-EB of dense NiTi free of cracks, solid cuboid NiTi specimens were fabricated on a freely programmable PBF-EB machine Freemelt One (Freemelt Holding, Mölndal, Sweden). The fixed process parameters for the sample fabrication are shown in Table 1.

In Table 1, l_{cube} and BH denote the lateral edge length and the height of the produced NiTi cuboids, respectively. For process development, the lateral velocity (v_{lat}) depending on the beam speed v_{beam} (see Eq. (1)) and the area energy (E_A) additionally depending on the power of the beam P_{beam} (see Eq. (2)) were varied to find suitable parameters to produce dense samples. The hatch-spacing l_0 was kept constant as shown in Table 1.

$$v_{lat} = \frac{v_{beam} \cdot l_0}{l_{cube}} \quad (1)$$

$$E_A = \frac{P_{beam}}{v_{beam} \cdot l_0} \quad (2)$$

To evaluate the printed parts' relative density, the microstructures of the cross-sections parallel to the build direction (z-direction) were analyzed through an optical microscope (AXIO Imager M1m, Carl Zeiss Jena GmbH, Germany). Prior to the microstructure analysis, the PBF-EB-produced cuboid samples were cut along the thickness direction (z) and polished with a 1 μm diamond finish. The area fraction of the misconnections is measured on binarized images of the cross-sections, and the relative density is calculated. Tensile tests were carried out according to DIN 50,125:2016–12 (Geometry B, M6) on an universal testing machine (Instron 4505 Retrofit, Instron Corporation, Canton, USA) at room temperature using a strain rate of 0.018 min^{-1}.

Thermomechanical compression cycling tests (training) were carried out on a Gleeble 3500 machine (Dynamic Systems Inc., Poestenkill, USA) using specimens prepared through PBF-EB and wire erosion according to the aspect ratio given in DIN 50,106:2016–11 (L = 14 mm, r = 3,5 mm). In this work, the unique test procedure developed on the Gleeble machine was used for the first time to determine the reversible strains caused by the phase transition. During the compressive tests on the Gleeble machine, the strain rate was set to 0.5 mm/min. The specimen was heated and cooled on the Gleeble machine using Joule heating at a constant stress of 25 MPa. The constant stress resulted from the preload of 0.5 kN which was necessary hold the specimen in a fixed position. The loading was released after the desired strain for each cycle was reached. This procedure was done on two specimens.

Table 1
Fixed process parameters for PBF-EB of Ti-rich NiTi samples on a Freemelt One machine.

Build temperature T_{build}	~ 820 °C
Scan pattern	Cross-snake hatching
Line-offset l_0	200 μm
Size of cuboid samples (l_{cube} × l_{cube} × BH)	10 × 10 × 15 mm^3
Layer height	75 μm

3. Results

3.1. PBF-EB processing window

To generate dense Ti-rich NiTi via PBF-EB, a processing map was determined as a function of area energy (2) and lateral velocity (1) (Fig. 1). The diagram on the left side of Fig. 1 displays the influence of the area energy and the lateral velocity on the relative density of the NiTi specimens. Red marks indicate specimens with insufficient energy input, resulting in porous samples with a relative density < 99.9%. In contrast, black triangular marks represent specimens with too high energy input and an uneven surface. The representative samples highlighted on the left side of Fig. 1 are further characterized in more detail (right). Top surface morphology and the microstructure of the cross-section parallel to the Build Direction (BD) are depicted on the right side to show the top surface evenness and the porosity of the different specimens produced using different processing parameters.

With increasing lateral velocity, the top surface evenness drops, and less area energy is required to gain dense NiTi. Dense NiTi samples can only be derived, when using appropriate PBF-EB process parameters.

3.2. Microstructure characterization

For the dense cuboid NiTi sample with an even top surface fabricated using an area energy of 1.25 J/mm^2 and a lateral velocity of 38 mm/s, the microstructure of the cross-section parallel to the build direction was analyzed (Fig. 2). Fig. 2 left shows the fine columnar morphology of the grains. These fine columnar grains grow in the direction parallel to the thermal gradient as well as to the BD. The sample is free of cracks and lack of fusion defects. Fig. 2 b middle depicts the microstructure with higher magnification, and the needle-like structure of the martensitic matrix inside the grains gets visible. The SEM analysis (Fig. 2 right) gives insight into the shape and the number of the precipitates. The lens-shaped precipitates are ~1 μm in width and between 3 μm and 10 μm in length. In addition, these precipitates are aligned along BD. Since the process temperature of ~820 °C lies in the two-phase area of NiTi and Ti_2Ni, the precipitates are assumed to be Ti_2Ni, which will be further discussed in Section 2.3 based on EPMA results.

3.3. Influence of segregation to the phase transition temperatures

The DSC and EPMA results for fresh and used powder as well as-built parts are shown in Fig. 3. The transition temperatures, the Ni-content and the oxygen content of these samples are summarized in Table 2. The DSC curves of the as-built sample exhibited a one-stage phase

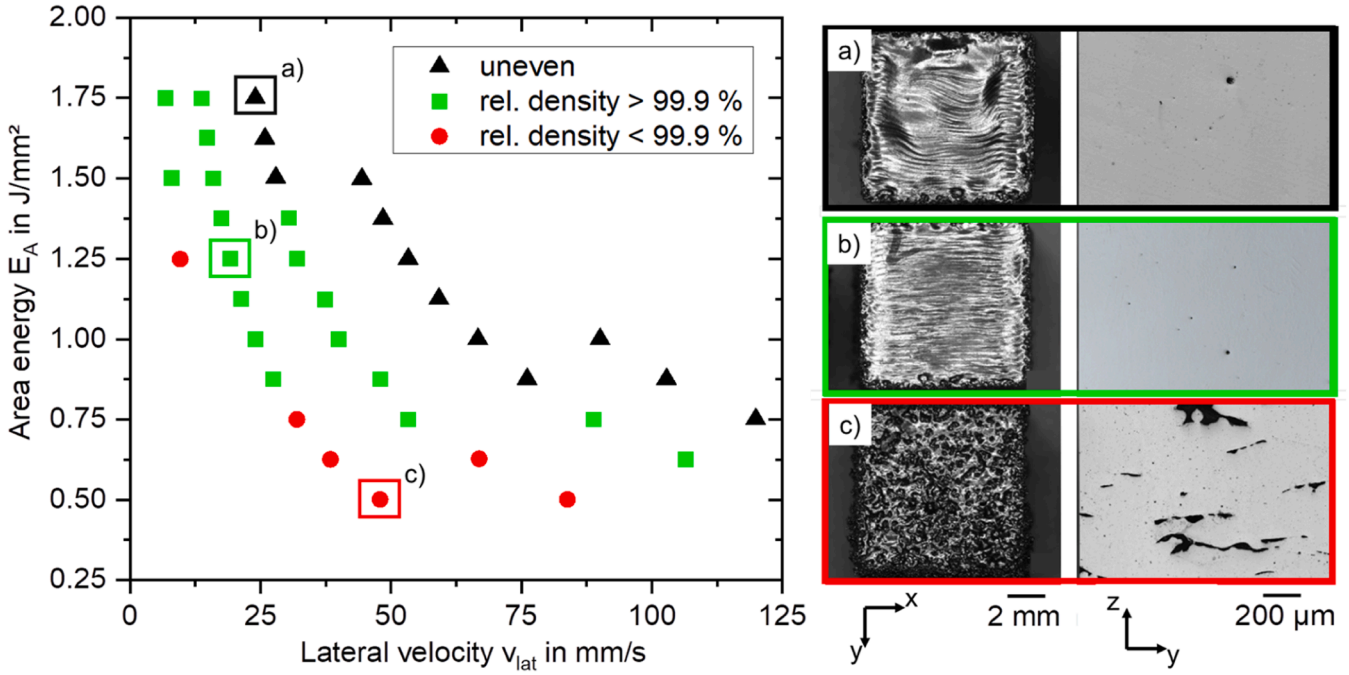

Fig. 1. Left Processing map for the fabrication of dense Ti-rich NiTi samples. Green marks represent cuboids with a relative density of > 99.9%, red marks display porous samples with density values of < 99.9% and black marks denote dense cuboids with an uneven top surface due to too high energy input. Right:Top view and cross-section of the PBF-EB-processed cuboids highlighted in the left diagram.

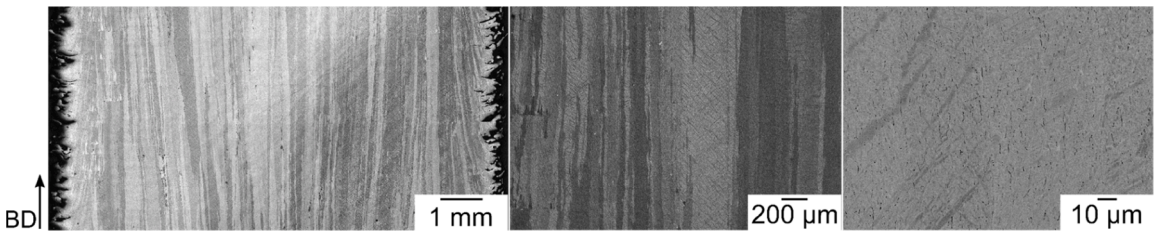

Fig. 2. Microsection parallel to the build direction (BD) of a cuboid sample built with an area energy of 1.13 J/mm^2 and lateral velocity of 37 mm/s. Left: Optical micrograph of the fine columnar microstructure. Middle: Optical micrograph focused on grains with martensitic needle-like microstructure. Right: SEM micrograph showing the shape, size and the number of the precipitates.

transition, while the powders showed a more complex DSC signal with more than one peak. Due to this, the austenite finish A_f and the martensite start temperature M_s are split up to analyze the phase transition behavior of the powders in more detail. $A_{f,1}$ represents the temperature where the first phase transition is finished; while $A_{f,2}$ displays the temperature where the martensite is completely converted into austenite. $M_{s,1}$ is the temperature at which martensite starts to form; while $M_{s,2}$ stands for the temperature where a second distinct phase transition starts. The austenite start temperature A_s and the martensite finish temperature M_f are used equivalent to literature. So, at A_s austenite starts to transform and below M_f only martensite is stable. The EPMA results display the local Ti composition in the respective microstructure for the three samples.

DSC signals (Fig. 3 left) of the two powders (red and black lines) show two peaks during heating and cooling. The transition temperatures of the samples are similar, but the intensities of the peaks are switched. During heating, the fresh powder shows a more prominent peak between A_s and $A_{f,1}$ and a smaller peak between $A_{f,1}$ and $A_{f,2}$ while the peak intensities of the aged powder reused for 20 EB-PBF process cycles are just contrary to those of the fresh powder. This effect of the changing peak intensities is also observable in the DSC cooling curve, while there is more like a shoulder between $M_{s,1}$ and M_f than two distinct peaks for the fresh powder.

Compared to the microstructure of the used powder (black framed image Fig. 3 right), the fresh powder (red framed) shows a high amount of interdendritic Ti-rich precipitates. If the powder particles get heated up to the build temperature of a PBF-EB process (~820 °C, see Table 1 homogenization of the microstructure is observed for the case of the used powder (black framed image in Fig. 3 right). The microstructure of the as-built sample (blue framed) shows a homogenous matrix with lens-shaped Ti-rich precipitates being considered to be Ti_2Ni or $Ti_4Ni_2O_x$.

3.4. Scheil solidification simulation (CALPHAD) of $Ni_{48.9}Ti_{51.1}$ (at.%)

For a better understanding of the evolution of the microstructures and the phase transitions, CALPHAD simulations were carried out. Since only the B2-matrix exhibits a martensitic phase transition in NiTi and not the Ti_2Ni precipitates, the Ni/Ti ratio in the matrix is the main contributor to the shift of the phase transition temperatures. In this study, in terms of simplicity, only the dependency on the Ni-content is shown. The results for the fresh $Ni_{48.9}Ti_{51.1}$ (at.%) powder are shown in Fig. 4 where the Ni-content in the B2-Matrix $x_{Ni,B2}$ and the mole fraction of solid are plotted over the decreasing temperature of the solidification.

To understand the powders' transition temperatures that do not agree with the previous research results for conventional NiTi, the rapid solidification and the resulting dendritic microstructure of the powder

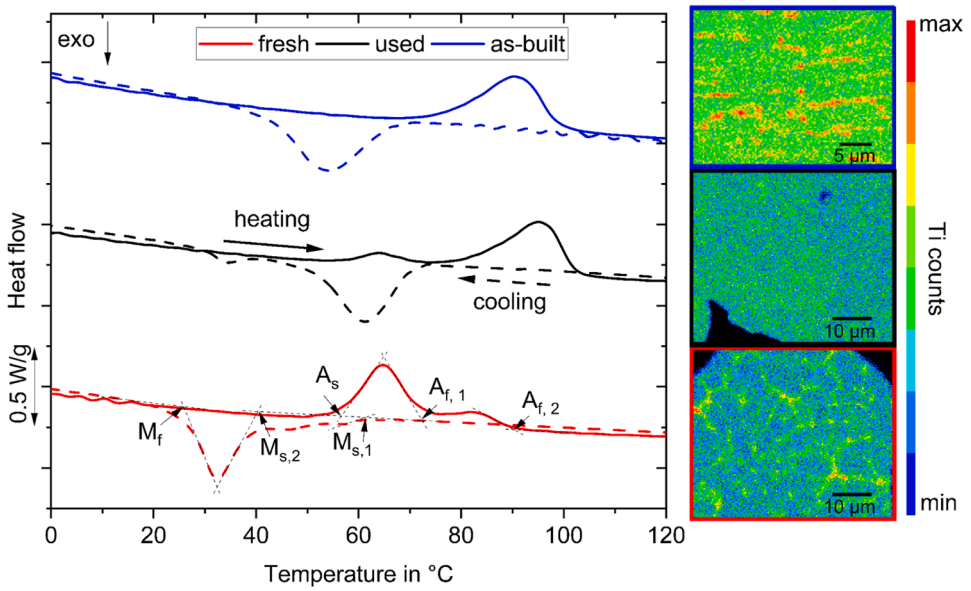

Fig. 3. Left: DSC curves of fresh and used powder as well as an as-built solid sample to analyze the phase transition temperatures which are summarized in Table 2:. In the powder samples, two peaks were detected, while the as-built sample only showed one peak. Right: EPMA results of the different samples.

Table 2
Nickel content analyzed using ICP-AES, oxygen content determined by means of EMGA and phase transition temperatures derived through DSC measurements utilizing the fresh and used powder and the solid samples built using PBF-EB.

Sample	Ni in at.%	O_2 in ppm	M_f* in °C	$M_{s,2}$ˆ in °C	$M_{s,1}$ˇ in °C	A_s‡ in °C	$A_{f,1}$† in °C	$A_{f,2}$ˈ in °C
Fresh powder	48.9 ± 0.3	386 ± 12	24.5	41.5	62.3	54.8	74.7	92.9
Used powder	48.7 ± 0.3	485 ± 19	29.5	45.0	70.5	56.1	78.6	102.6
As-built bulk	48.1 ± 0.1	798 ± 30	41.5	–	67.1	74.2	99.4	–

* M_f: Martensite finish temperature.
ˆ $M_{s,2}$:Second martensite start temperature.
ˇ $M_{s,1}$: First martensite start temperature.
‡ A_s: Austenite start temperature.
† $A_{f,1}$: First austenite finish temperature.
ˈ $A_{f,2}$: Second austenite finish temperature.

have to be taken into account. The matrix of the fresh powder starts to solidify with a Ni-content of 50.2 at.% ($x_{Ni,dendr}$) at a liquidus temperature of 1307 °C. Until a temperature of 986 °C only the B2-matrix crystallizes. The last 8 mol.% of solid at the temperatures of 986 °C – 982 °C corresponds to the Ti_2Ni precipitation. When the solidus temperature of the material ($T_{solidus}$ = 982 °C) is reached, the Ni composition of the matrix reaches a value of 49.3 at.% ($x_{Ni,hom}$).

3.5. Tensile properties at room temperature

The tensile tests were carried out to determine the mechanical behavior of the as-built NiTi and to compare the results to other additive manufacturing processes. The stress-strain curve for as-built Ti-rich NiTi at room temperature is shown in Fig. 5 on the left side. On the right side of Fig. 5, a representative overview of a fractured surface with highlighted features is displayed. Table 3 summarizes the so-measured material characteristics.The total elongation of the samples is 5.2%, while the ultimate tensile strength is about 736 MPa. There is no distinct stress plateau, and no necking was observable after the fracture. Nevertheless, a detwinning and reorientation region between 1.0 – 3.5% can be observed.

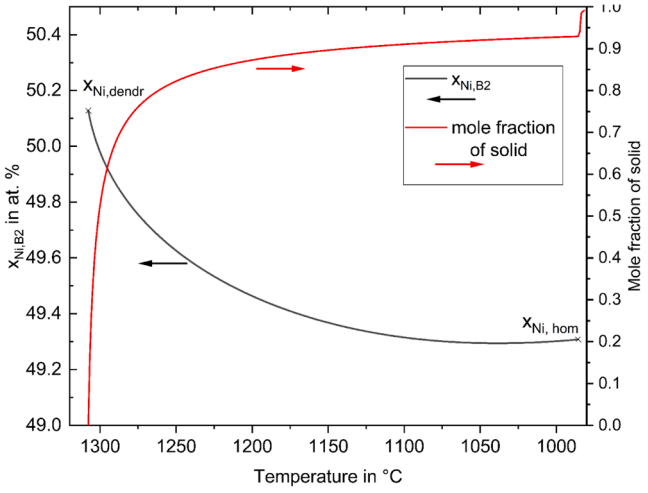

Fig. 4. CALPHAD Scheil calculation of the solidification of Ni48.9Ti51.1 (at. %). The Ni-content of the B2-matrix (black curve) and the mole fraction of solid (red curve) are shown over the decreasing temperature. The Ni content decreases until 1050 °C while the mole fraction of the solid increases steeply to 0.7% from 1307 °C to 1280 °C. Ti2Ni precipitates after 985 °C up to an amount of 8 mol.%.

The overview of the fracture surface exhibits a quasi-cleavage pattern. In addition, microcracks (red framed) are seen and a very fine dimple structure (black framed) gets visible under higher magnification.

3.6. Thermomechanical compression properties

To analyze the functional properties of the PBF-EB-printed NiTi, thermomechanical cycling is a useful tool. For Ti-rich NiTi, the shape memory effects are of main interest. This unique experiment setup executed on the Gleeble 3500 offers the possibility to characterize the reversible strains resulting from the martensitic phase transformation. So, the reversible strain in the martensite and the austenite phase as well as a TWSM strain can be measured since the strain and the temperature is accessible throughout the loading, unloading, heating and cooling. In addition, the influence of the strains on the transformation temperatures

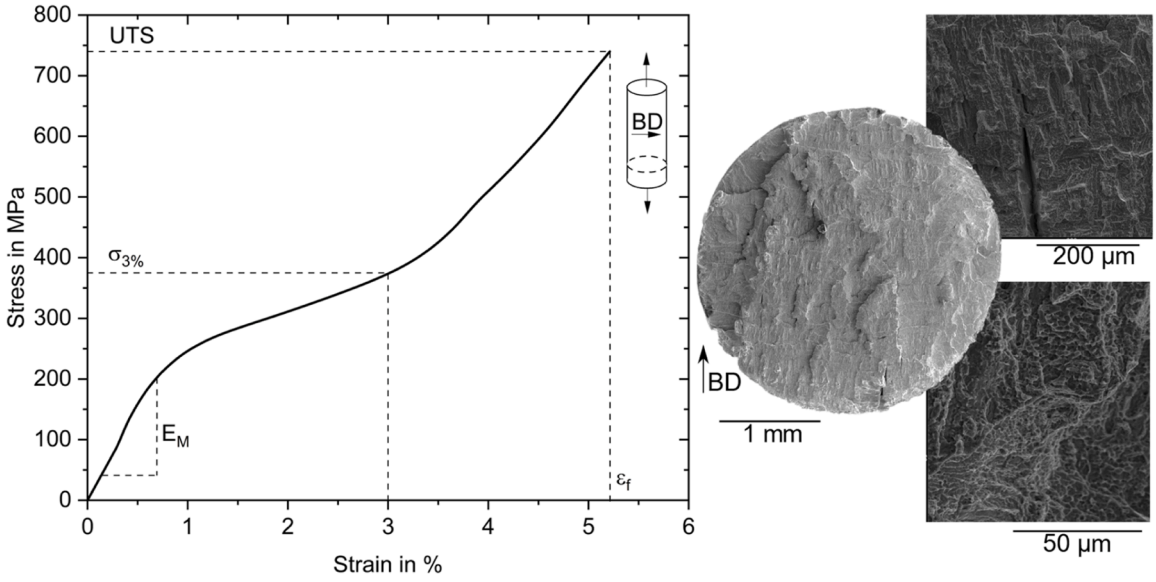

Fig. 5. Left: Stress-strain curve derived by the room temperature tensile test of the as-built NiTi. Right: Overview of the fracture surface. Microcracks (red framed) in a very fine dimple structure (black framed) are observable.

Table 3
Tensile test results of PBF-EB-produced NiTi in the as-built state.

Stress at 3% strain $\sigma_{3\%}$	374 ± 1 MPa
Ultimate Tensile Strength, UTS	735 ± 8MPa
Fracture elongation ε_f	5.2% ± 1

can be calculated, but the focus of this study is set to the shape memory strain analysis.

Fig. 6 a shows a schematic of the stress-strain-temperature curves for the first compression and heating cycles ($n \leq 3$) of an as-built Ti-rich NiTi. After cooling below M_f (point 1 in Fig. 6 a, for the first cycle, i.e., $n = 1$), the sample is compressed up to desired strain ε (point 2), unloaded (point 3), and heated up under constant stress of 25 MPa to a temperature higher than A_f (point 4). While compression, the material first deforms elastically; then, a strain plateau is detected due to detwinning and reorientation; and subsequently, slip occurs. To analyze the strains due to SME, the TWSM strain ε_{TWSM}, the irreversible strain in austenite $\varepsilon_{A,irr}$ in martensite $\varepsilon_{M,irr}$ and the reversible strain at room temperature $\varepsilon_{M,rev}$ are plotted over the cycles. The TWSM strain ε_{TWSM} is defined as the difference between the strains at 140 °C (point 4) and the strain after cooling (point 1′ for the second cycle, i.e., $n = 2$ in Fig. 6 a) since only a temperature difference leads to the shape change. The Arabic numerals with the prime symbol(s) represent the corresponding status after defined compression cycles, n. The irreversible strain of austenite $\varepsilon_{A,irr}$ is the change of the strains from point 4′ and the preceding cycle at 140 °C (point 4); while the irreversible strain of martensite $\varepsilon_{M,irr,n}$ is the difference of the stains at room temperature

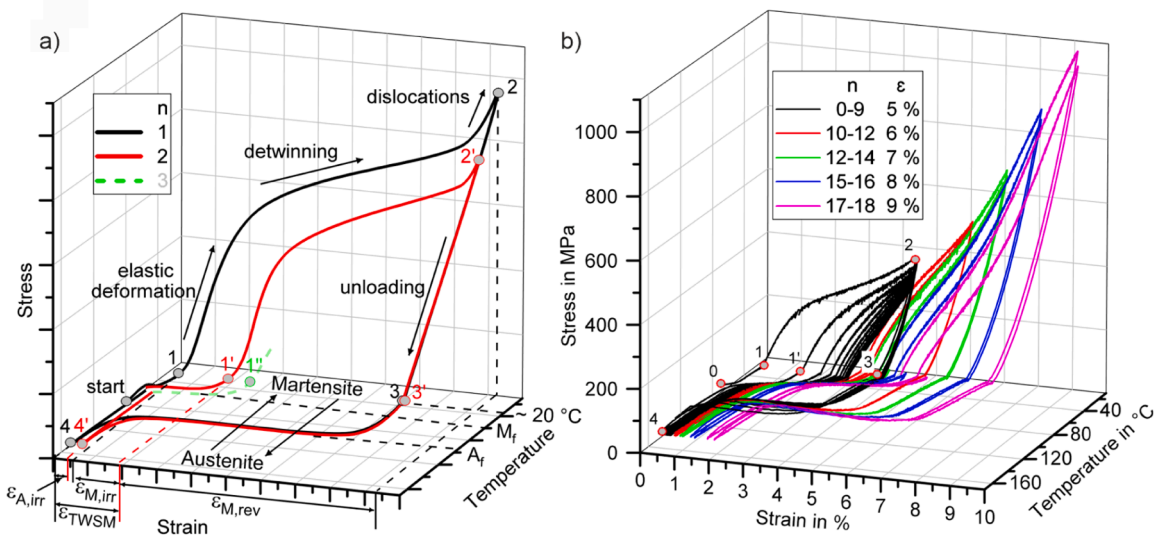

Fig. 6. (a) Schematic stress-strain-temperature curves over the first compression and heating cycles ($n \leq 3$) for an as-built Ti-rich NiTi sample. The strain of the sample is set to zero while the austenite (temperature > A_f) is stable (start point). After cooling below M_f (point 1), the sample is compressed up to point 2. Subsequently, the sample is unloaded (point 3) and at the end of each cycle, the sample is heated up to a temperature higher than A_f (point 4). This method allows for the analysis of the strains due to SME and the loading behavior.
(b): Measured stress-strain-temperature curves for the as-built PBF-EB NiTi over 19 compression cycles. The colors represent different process cycles, where the sample is trained to desired strain values. The numbered points are used equivalent to (a).

(point 1′ and 1). The reversible $\varepsilon_{M,rev}$ is defined by the point where the maximum stress was achieved (point 2) and the loading point of the following cycle (point 1′). Fig. 6 b shows the measured stress-strain-temperature curves for the as-built PBF-EB NiTi over 19 compression cycles ($n = 19$).

When looking at the measured stress-strain curve shown in Fig. 6 b, a detwinning region is observable, but no distinct stress plateau is reached. In addition, the stress plateau diminishes over the cycle number. OWSME ($\varepsilon_{M,rev}$) as well as TWSME (ε_{TWSM}) of Ti-rich NiTi processed via PBF-EB are detectable.

A more detailed analysis of the predefined reversible and irreversible strains over the cycles is shown in Fig. 7. At the 0 cycle, the specimen was only thermally treated at a constant compressive load of 25 MPa, and a $\varepsilon_{TWSM,0}$ (1′−4) of 0.5% was detected. Furthermore, one can see in the first three cycles that $\varepsilon_{M,irr}$ (green triangles) decreases by 0.9%, while ε_{TWSM} (black squares) shows an increase by 1.2% which almost covers the combined irreversible strain. Between cycles 3 and 10, TWSME with ε_{TWSM} of ~2.4% is more prominent than OWSME with $\varepsilon_{M,rev}$ of ~1.7%. In addition, a steady state for the irreversible strains ($\varepsilon_{M,irr}$ and $\varepsilon_{A,irr}$) is observed, but still, the martensite and austenite combined irreversible strains show functional fatigue of ca. 0.1% at each cycle which leads to a steady decrease of $\varepsilon_{M,rev}$. For cycles $n > 10$, the desired strain increased stepwise. As a result, the irreversible strains ($\varepsilon_{M,irr} + \varepsilon_{A,irr}$) of each cycle tend to grow, while $\varepsilon_{M,rev}$ considerably increases. For $3 < n < 10$ a constant shape recovery in average > 95% was reached. Still after 19 cycles and a desired strain of 9%, a shape recovery of > 90% was achieved.

4. Discussion

4.1. Process parameter for dense Ti-rich NiTi via PBF-EB

First, a processing map as a function of area energy and lateral velocity was chosen to display the influence of process parameters on the porosity, since it displays the parameters independent from the scan length and can represent the time of return being important for the melt pool formation [15]. Ti-rich NiTi shows a “banana-shaped” PBF-EB processing window (Fig. 1) with porous, dense and uneven regions, being very similar to that in the case of PBF-EB of Ti-6Al-4 V [16] or stainless steel [17]. Insufficient energy input results in lack of fusion defects and porous samples with a relative density of < 99.9%. Cross-sections of specimens produced using too high energy input appear dense, but the recoil pressure during evaporation leads to an increased melt pool movement and finally to a rough and uneven surface [16]. Furthermore, the stability of the melt pool believed to be highly connected to the generation of a PBF-EB process window. A partial persistent melt pool can lead to a pile up of material and lead to bulging, other than a trailing melt pool. With higher velocity the creation of a persistent melt pool is reached at lower area energy. [18] Such a surface should be avoided in terms of the geometric accuracy of samples and process stability. Between the uneven and the porous samples, a dense region with an even surface opens up. In literature equiatomic PBF-EB NiTi samples with a rel. density higher than 98% measured using the Archimedes principle were achieved for comparable area energies (~1.25–2.5 J/mm^2) for lateral velocities lower than 20 mm/s. [12]

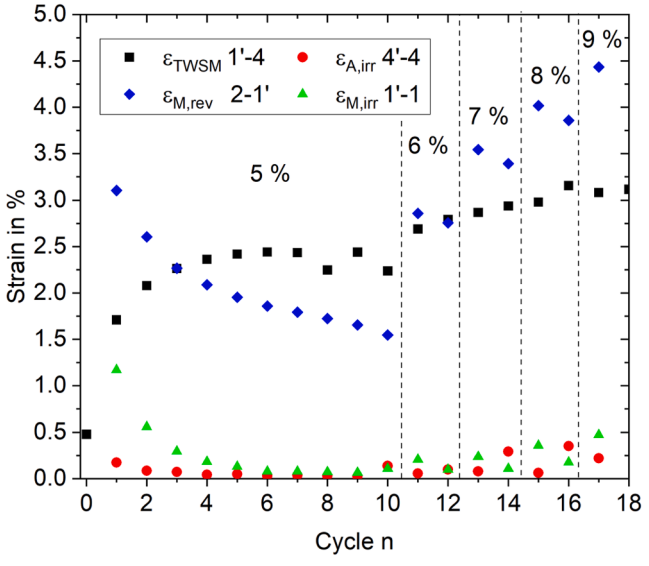

Fig. 7. The irreversible strains at martensite $\varepsilon_{M,irr}$ (4′ – 4) and austenite $\varepsilon_{A,irr}$ (1′ – 1) as well as the reversible strains due to TWSM strain ε_{TWSM} (1′ – 4) and OWSME ($\varepsilon_{M,rev}$) are plotted over the 19 cycles. For the first ten cycles (n: 0 – 9), the built NiTi sample was trained up to a desired strain of 5%; while in the following thermomechanical cycles (n: 10 – 12, n: 13 – 14, n: 15 – 16, n: 17 – 18), the predefined strain increased stepwise up 9% as already shown in 3D in Fig. 6.

In all samples, gas porosity was observed, which is defined by the round shape of the pores. These pores originate from the gas inside powder particles and rely mainly on the powder quality. This porosity cannot be avoided with optimized PBF-EB process parameters [7,18].

The PBF-EB-produced dense NiTi shows a typical fine columnar grain structure (Fig. 2), which is attributed to the thermal gradient parallel to BD [11,12,15]. According to the literature [19] and the CALPHAD simulation results (2.4), the Ti-rich NiTi used in this study should have ca. 8 mol.% Ti_2Ni precipitates which were observed via microscope inside the grains and at the grain boundaries. In addition, the relatively high oxygen content of 798 ppm can lead to the formation of complex $Ti_4Ni_2O_x$ phases [10]. Those two phases cannot be distinguished via crystallographic analysis. Since the ratio between Ti and Ni is equal for these Ti_2Ni and $Ti_4Ni_2O_x$; also EPMA is not a helpful tool to tell them apart [19]. Both phases should strengthen the NiTi due to precipitation hardening effects while the material still shows a good shape recovery [20]. Beside this effects, the high number of precipitates could even reduce the negative influence of a high oxygen pickup since the Ti_2Ni phase can solute oxygen and form $Ti_4Ni_2O_x$ [20]. Due to the high amount of precipitates in this alloy the overall number of precipitates is not expected to increase with a higher oxygen content. The occurrence of the Ti_2Ni phase was also found by other studies in PBF-EB using equiatomic NiTi powder [12].

4.2. Martensitic phase transition in powder and parts

In Fig. 8, $M_{s,1}$ and $M_{s,2}$ derived by means of DSC (see Fig. 3) are compared with literature data [13] and set in context with the Ni-content measured via ICP-AES (see Table 2) and calculated with CALPHAD (see Fig. 4)

Fig. 8 shows that $M_{s,1}$ for all three samples fit within a 90% confidence fit of the literature data derived by Farber et al. [13]. However, $M_{s,2}$ plotted with the overall Ni-content of the powder measured using ICP-AES is located in the lower area outside the gray region. The 90% confidence interval was chosen, since a standard deviation up to 9 °C for the phase transition temperatures determined via DSC can be considered [21]. If the phase transition temperatures of the $M_{s,2}$ marks is projected to boundaries of the gray region, the derived Ni-content would fit to the calculated $x_{Ni,dendr}$. With this diagram, the martensitic phase transition for the powders with several peaks and the one-stage phase transition of the as-built part can be well explained.

Since the majority of the fresh powder particles underwent a rapid solidification during the powder production process based on the atomization with a high cooling rate of 10^6–10^8 K/s [22], the Scheil segregation effect resulting in an enrichment of Ni ($x_{Ni,dendr}$) in the matrix is not negligible. Due to the inhomogeneous distribution of the Ni-content in the dendritic core and interdendritic area, more than one distinct DSC peaks were observed in the case of the fresh powder. The

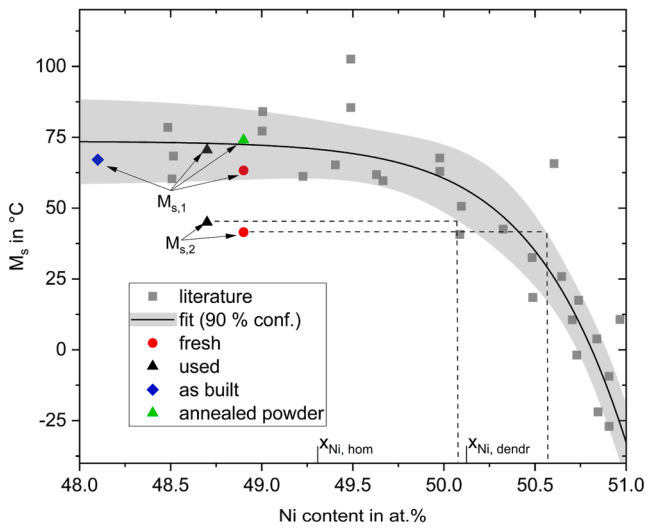

Fig. 8. $Ms_{,1}$ and $M_{s,2}$ measured via DSC are plotted as a function of the global Ni-content of the samples measured via ICP-AES and compared with literature data [11] with a 90% confidence interval. The blue rhombus denotes the as-built part containing ~48.1 at.% of Ni, while the red points and black triangles represent fresh and used powder with a Ni-content of ~48.9 at.% and ~48.7 at.%, respectively. The green triangle shows an annealed fresh powder using a furnace for 4 h at 1000 °C. Furthermore, $x_{Ni,dendr}$ of 50.13 at.% and $x_{Ni, hom}$ of 49.29 at.%, are calculated using CALPHAD.

used powder particles were partially heated up to the build temperature, at which the precipitates dissolved and the Ni/Ti ratio in the matrix reached the homogenous composition ($x_{Ni,hom}$). The precipitates change their shape to small round particles which are too small to detect via EPMA. However, not all powder particles did see an elevated temperature even after 20 PBF-EB processes while they remained in the dendritic microstructure. So it can be concluded that the peak with $M_{s,2}$ of the powder samples results from the dendritic particles with $x_{Ni,dendr}$ and the second peak originates from the homogenous particles with $x_{Ni,hom}$. To confirm the founding, a DSC measurement was performed on an annleaed (1050 °C; 2.5 h) powder. The signal showed a one peak transition and the M_s was in the temperature region for equilibrium NiTi. In addition, the increased oxygen content which mainly locates in the skin area around the powder particles could lead to the formation of Ti-rich oxygen phases; thus, precipitates were barely observable in internal region inside the powder particles.

The as-built sample shows a one-step transition which is in good agreement with the literature data when considering the overall Ni-content measured via ICP-AES. The PBF-EB-produced sample exhibits more Ti-rich precipitates in the microstructure compared to the used powder, which can also result from the Ni-loss (0.6 at.%) of the PBF-EB process [9].

Obeidi et al. [23] and Walker et al. [24] also observed a complex DSC signal with more than one distinct peak in the fresh powder, which were explained by the presence of a R-phase; Khoo et al. [25] mentioned that NiTi was sensitive to local change in the chemical composition which could lead to the observation of more peaks in the DSC signal. Based on the results derived in this work, the presence of several DSC peaks in NiTi powder is systematically explained and is considered to result from the segregation induced by the high solidification rate during powder atomization.

4.3. Mechanical properties of PBF-EB-produced Ti-rich NiTi

The PBF-EB-processed NiTi in the as-built state showed a microstructure enriched with precipitates (Fig. 3 right); thus, during the tensile test (Fig. 5 left), the formation of a stress plateau was not observed due to local slip before the yield strength was reached [26]. The fractured surface represented a typical quasi-cleavage pattern for Ti-rich NiTi (Fig. 5 left), which was also reported in the literature [27]. The fracture behavior is a conjunction of cleavage and ductile fracture but is dominated by the brittle fracture. Comparable observations were gained in the case of Ni-rich precipitate-hardened NiTi [28]. Compared to other NiTi samples produced in previous works using PBF-EB, Hayat et al. observed lower values in strength and elongation [29], while Zhou et al. [10] achieved higher strength of 1411 MPa and elongation (11%) using a superelastic Ni-rich NiTi alloy. The improved mechanical properties observed by Zhou et al. could be explained by the lower oxygen content (500 ppm) and the higher Ni-content [10]. In the case of NiTi produced by means of PBF-L, comparable total elongation and higher UTS were reported, if produced with very low oxygen pickup [9]. As a result, the main contributor to worsening the mechanical properties of PBF-L samples is thought to be high oxygen pickup [2,9]. Consequently, cracks and pores should also have an inferior influence on the material properties of the PBF-EB as-built NiTi presented in this study than the high number of precipitates from the high Ti-content.

The deformation behavior during compression tests is comparable to the observations derived during the tensile test (Fig. 6). The precipitations lead to the hardening of the material, and accumulating stress fields could create a slip, even before the yield strength is reached [26].

Furthermore, the same tension-compression asymmetry described by Zhou et al. [10] for Ni-rich PBF-EB NiTi was also found to be present in this study. In the literature, it is well known that NiTi exhibits (001)-direction in the austenite after PBF-EB [12] and shows hard properties in tension while soft properties in compression [30]. So, it can be concluded that the microstructure of the PBF-EB-produced Ti-rich NiTi might exhibits as well an (001) texture.

4.4. Functional properties of PBF-EB-produced Ti-rich NiTi

The increase of the irreversible $\varepsilon_{M,irr}$ combined with a decrease of the reversible strain in the martensite state $\varepsilon_{M,rev}$ at the first cycles and a constant reversible strain rate of 95% after 3 cycles were measured via thermo-mechanical cycling tests (Fig. 7). Similar results were also measured by Haberland et al. for conventional and PBF-L-processed NiTi samples where the irreversible strain was accumulating in the first loading cycles while they decay after several cycles [31]. The decay of the $\varepsilon_{M,rev}$ in the first cycles is attributed to residual strains and resulting from slip before reaching yield strength [32]. The accumulating irreversible strain while cycling at stresses lower than the yield point due to localized slip deformation caused by internal stresses represents a difficulty for shape memory applications of NiTi and should be as low as possible [31,32]. In addition, TWSME is connected to local internal stresses mostly resulting from thermomechanical training under constant stress. This training creates a dislocation structure with local internal stress fields in the NiTi sample. The stress fields guide the martensite reorientation after the phase transition [33]. Precipitates have a major influence on localized internal stress fields and could influence the functional properties of NiTi [26,34]. Even without any training cycles, ε_{TWSM} of 0.5% with a nonlinear increase of this effect in the first three cycles was seen to be present. Residual stresses, texture, precipitates and defects from the process could lead to those effects [33,35,36]. Since it was found out that the irreversible strain in martensite at the first cycles is directly transformed into the TWSME strain, the extensive training of the material could be optimized with a tailored microstructure. Nevertheless, further research has to be done to evaluate the influence of the effect of the microstructure on the TWSME. For $n > 3$, a linear increase in ε_{TWSM} was observed, which can be expected for this pre-deformations of the martensite compared with the study from Liu et al. [33].

5. Conclusion

In this study, dense Ti-rich NiTi was processed using PBF-EB and characterized via tensile testing as well as a new approach for thermomechanical cycling was carried out. In the microstructure of PBF-EB-fabricated NiTi, typical columnar grains parallel to the building direction with a high amount of textured Ti-rich precipitates were observed. This precipitation results from the high Ti-content of the used powder.

The transition temperatures of the as-built NiTi are comparable to the conventional fabricated NiTi. However, the powder samples showed DSC signals with several peaks, which did not fit with the literature data about conventional NiTi. Based on EPMA, CALPHAD as well as literature research results, the presence of more DSC peaks for Ti-rich NiTi powders is explained by the segregation induced by the high solidification rate during the powder manufacturing process.

The high number of precipitates induced a hardening effect, resulting in an indistinct stress plateau. Thermomechanical cycling offered the opportunity to measure the reversible strains and phase transition temperatures in-situ. A combined reversible strain (OWSME and TWSME) of ~7.5% after 19 thermomechanical cycles was measured. Furthermore, it was observed that the irreversible strain in the first thermomechanical cycles is only measured in the martensitic state while in the austenitic state the material exhibited almost complete shape recovery. Therefore, the irreversible strain in austenite is almost completely converted in the TWSM strain from the first cycle on. This training effect could be intensified due to the precipitates, texture or internal stresses from the building process, where further research has to be done to understand this relationship between the SME and PBF-EB NiTi.

Funding

Financial support from the German Research Foundation (DFG, Deutsche Forschungsgemeinschaft, Bonn, Germany; project number: 432515505) is gratefully acknowledged.

Declaration of Competing Interest

We declare that we have no financial and personal relationships with other people or organizations that can inappropriately influence our work, and there is no professional or other personal interest of any nature or kind in any product, service, and/or company that could be construed as influencing the position presented in, or the review of the manuscript entitled “Functional properties and shape memory effect of Nitinol manufactured via electron beam powder bed fusion”.

Acknowledgments

We are grateful to Sabine Michel, Kerstin Zinn und Annemone Alleborn for performing the sample preparation and microstructure characterization by SEM. In addition, we thank the colleagues from the institute of “Chemical Reaction Engineering” (FAU) for giving the possibility for DSC measurements and performing the ICP-AES. Eventually, we acknowledge the fruitful cooperation with the chair “Reaction Engineering and Catalysis” at the TU-Dortmund, with the project partners Dominik Rudolf and Prof. Hannsjörg Freund.

References

[1] D.C. Lagoudas, Shape Memory Alloys: Modeling and Engineering Applications, Springer US, 2008.
[2] M. Elahinia, N. Shayesteh Moghaddam, M. Taheri Andani, A. Amerinatanzi, B. A. Bimber, R.F. Hamilton, Fabrication of NiTi through additive manufacturing: a review, Prog. Mater Sci. 83 (2016) 630–663.
[3] M.H. Elahinia, M. Hashemi, M. Tabesh, S.B. Bhaduri, Manufacturing and processing of NiTi implants: a review, Prog. Mater Sci. 57 (2012) 911–946.
[4] G. Costanza, M.E. Tata, Shape memory alloys for aerospace, recent developments, and new applications: a short review, Materials (Basel, Switzerland) (2020) 13.
[5] L. Seigner, O. Bezsmertna, S. Fähler, G.K. Tshikwand, F. Wendler, M. Kohl, Origami-inspired shape memory folding microactuator 2020 6.
[6] A. Fink, Electron beam based additive manufacturing of auxetic structures composed of shape memory Nitinol as catalyst carrier, in: ESMC2022.
[7] Z. Fu, C. Körner, Actual state-of-the-art of electron beam powder bed fusion, Eur. J. Mater. 2 (2022) 54–117.
[8] M.R. Hassan, M. Mehrpouya, S. Dawood, Review of the machining difficulties of nickel-titanium based shape memory alloys, AMM 564 (2014) 533–537.
[9] X. Wang, J. Yu, J. Liu, L. Chen, Q. Yang, H. Wei, J. Sun, et al., Effect of process parameters on the phase transformation behavior and tensile properties of NiTi shape memory alloys fabricated by selective laser melting, Addit. Manuf. 36 (2020), 101545.
[10] Q. Zhou, M.D. Hayat, G. Chen, S. Cai, X. Qu, H. Tang, P. Cao, Selective electron beam melting of NiTi: microstructure, phase transformation and mechanical properties, Mater. Sci. Eng.: A 744 (2019) 290–298.
[11] P. Krooß, C. Lauhoff, T. Gustmann, T. Gemming, C. Sobrero, F. Ewald, F. Brenne, et al., Additive manufacturing of binary Ni–Ti shape memory alloys using electron beam powder bed fusion: functional reversibility through minor alloy modification and carbide formation, Shap. Mem. Superelasticity 8 (2022) 452–462.
[12] Z. Lin, Influence of electron beam powder bed fusion process parameters on transformation temperatures and pseudoelasticity of shape memory nickel titanium.
[13] E. Farber, J.N. Zhu, A. Popovich, V. Popovich, A review of NiTi shape memory alloy as a smart material produced by additive manufacturing, Mater. Today: Proc. 30 (2020) 761–767.
[14] J. Frenzel, E.P. George, A. Dlouhy, C. Somsen, M.X. Wagner, G. Eggeler, Influence of Ni on martensitic phase transformations in NiTi shape memory alloys, Acta Mater. 58 (2010) 3444–3458.
[15] J. Pistor, C. Breuning, C. Körner, A single crystal process window for electron beam powder bed fusion additive manufacturing of a CMSX-4 Type Ni-based superalloy, Materials (Basel, Switzerland) (2021) 14.
[16] A.M. Rausch, V.E. Küng, C. Pobel, M. Markl and C. Körner, Predictive simulation of process windows for powder bed fusion additive manufacturing: influence of the powder bulk density (2017) 1117.
[17] S. Roos, L.E. Rännar, Process window for electron beam melting of 316LN stainless steel, Metals (Basel) 11 (2021) 137.
[18] Christoph Breuning, Julian Pistor, Matthias Markl and Carolin Körner, Basic mechanism of surface topography evolution in electron beam based additive manufacturing.
[19] B. Bertheville, J.E. Bidaux, Alternative powder metallurgical processing of Ti-rich NiTi shape-memory alloys, Scr. Mater. 52 (2005) 507–512.
[20] H.C. Lin, S.K. Wu, J.C. Lin, The martensitic transformation in Ti-rich TiNi shape memory alloys, Mater. Chem. Phys. (1994) 184–190.
[21] F. Sczerzenie, Consideration of the ASTM Standards for Ni - Ti Alloys 2004.
[22] E.J. Lavernia, T.S. Srivatsan, The rapid solidification processing of materials: science, principles, technology, advances, and applications, J. Mater. Sci. 45 (2010) 287–325.
[23] M.A. Obeidi, M. Monu, C. Hughes, D. Bourke, M.N. Dogu, J. Francis, M. Zhang, et al., Laser beam powder bed fusion of nitinol shape memory alloy (SMA), J. Mater. Res. Technol. 14 (2021) 2554–2570.
[24] J. Walker, C. Haberland, M.T. Andani, H.E. Karaca, D. Dean, M. Elahinia, Process development and characterization of additively manufactured nickel–titanium shape memory parts 2016 2653–2660.
[25] Z.X. Khoo, J. An, C.K. Chua, Y.F. Shen, C.N. Kuo, Y. Liu, Effect of heat treatment on repetitively scanned SLM NiTi shape memory alloy, Materials (Basel) 12 (2018) 77.
[26] K. Johansen, H. Voggenreiter, G. Eggeler, On the effect of TiC particles on the tensile properties and on the intrinsic two way effect of NiTi shape memory alloys produced by powder metallurgy, Mater. Sci. Eng. (1999) 410–414. A 273-275.
[27] J.H. Chen, G.Z. Wang, W. Sun, Investigation on the fracture behavior of shape memory alloy NiTi, Metall. Mat. Trans. A 36 (2005) 941–955.
[28] K. Gall, N. Yang, H. Sehitoglu, Chumlyakov, I. Yuriy, Fracture of precipitated NiTi shape memory alloys, Int. J. Fract. (2001) 189–207.
[29] M.D. Hayat, G. Chen, N. Liu, S. Khan, H.P. Tang, P. Cao, Physical and tensile properties of NiTi alloy by selective electron beam melting, Key Eng. Mater. (2018) 148–154.
[30] K. Gall, H. Sehitoglu, Y.I. Chumlyakov, I.V. Kireeva, Tension–compression asymmetry of the stress–strain response in aged single crystal and polycrystalline NiTi, Acta Mater. 47 (1999) 1203–1217.
[31] Christoph Haberland, Mohammad Elahinia, Jason Walker, Horst Meier, Jan Frenzel, Additive manufacturing of shape memory devices and pseudoelastic components, in: Proceedings of the ASME 2013, 2013.
[32] W. Zaki, Z. Moumni, A 3D model of the cyclic thermomechanical behavior of shape memory alloys, J. Mech. Phys. Solids 55 (2007) 2427–2454.
[33] Y. Liu, Y. Liu, J. van Humbeeck, Two-way shape memory effect developed by martensite deformation in NiTi, Acta Mater. 47 (1998) 199–209.
[34] H. Scherngell, A. Kneissl, Influence of the microstructure on the stability of the intrinsic two-way shape memory effect, Mater. Sci. Eng.: A (1999) 400–403, 273-275.
[35] K.C. Atli, I. Karaman, R.D. Noebe, D. Gaydosh, The effect of training on two-way shape memory effect of binary NiTi and NiTi based ternary high temperature shape memory alloys, Mater. Sci. Eng.: A 560 (2013) 653–666.
[36] A. Falvo, F.M. Furgiuele, C. Maletta, Functional behaviour of a NiTi-welded joint: two-way shape memory effect, Mater. Sci. Eng.: A (2008) 647–650, 481-482.